Indium based metal-organic framework/carbon nanotubes composite as a template for In2O3 porous hexagonal prisms/carbon nanotubes hybrid structure and their application as promising super-capacitive electrodes

Fatemeh Farbod a, Mohammad Mazloum-Ardakani a,*, Hamid Reza Naderi b, Ali Mirvakili c,
Mengjiao Wang d, Dipak V. Shinde d, Silvia Dante e, Pejman Salimi f,g, Simone Lauciello h,
Mirko Prato e

a *Department of Chemistry, Faculty of Science, Yazd University, Yazd, 89195-741, Iran*
b *Novin Ebtekar Company, Exclusive Agent of Metrohm-Autolab and Dropsens Companies, East Hagh Talab St. South Allame St.9 Saadat abad Ave., Tehran*
1997834991, Iran
c *Department of Electrical Engineering, Yazd University, Yazd, 89196-741, Iran*
d
Department of Nanochemistry, Istituto Italiano di Tecnologia, via Morego 30, 16163 Genova, Italy
e *Materials Characterization Facility, Istituto Italiano di Tecnologia, via Morego 30, 16163 Genova, Italy*
f *Istituto Italiano di Tecnologia, via Morego 30, Genova 16163, Italy*
g *Department of Chemistry and Industrial Chemistry, University of Genova, via Dodecaneso 31, I-16146 Genova, Italy*
h *Electron Microscopy Facility, Istituto Italiano di Tecnologia, via Morego 30, 16163 Genova, Italy*

Keywords: Hexagonal, MI 68 (In) prisms, Interweaved MOF with CNTs, Symmetric supercapacitor

A B S T R A C T

The development of porous nano/microsctructural materials, has a major focus to provide impressive electrochemical features in energy storage technology. Metal-organic frameworks (MOFs) are emerging as talented materials in supercapacitors due to their intrinsic porosity properties, which can be well-controlled through molecular engineering. As smart pathways, utilizing MOFs as templates for generating carbon, metal oxide, and hydroxides, etc. materials, or hybridized MOFs have shown to be quite beneficial. MOF Hybridizing with carbon nanotubes helps considerably eliminate the defects of pristine MOFs and enlargement the capacity to a certain extent which accounts for the increment of conductivity and electron/ion transports capability. Furthermore, adding hierarchy to the MOFs structure using incorporating of carbon nanotubes can improve composite stability. Herein we synthesized interweaved MIL 68 (In) with multi wall carbon nanotubes (MIL 68 (In)-CNTs) composite and also we employ it as a template for In2O3 porous hexagonal prisms hybridized with carbon nanotubes (In2O3 PHP-CNTs). Facile solvothermal method and simple annealing treatment are used for these approaches. We investigate their electrochemical performance using a three-electrode cell system. Using cyclic voltammetry (CV) technique, MIL 68 (In)-CNTs electrode modifier exhibit the superior capacity of 601 Fg- 1 at the speed rate of 5 mVs- 1. Besides, we assemble the symmetric supercapacitor (SSC) device via the MIL 68 (In)-CNTs nano platform. The synergistic effect between MIL 68 (In) and CNTs brings forth to an improved electrochemical performance with high energy and power density values of 13.3 Whkg- 1 and 300 Wkg- 1, respectively. This device shows high specific capacitance of 314 Fg- 1 at 0.5 Ag- 1, good rate capability and excellent cycling stability of 95% after 4000 cycles.

Introduction

Supercapacitors (SCs), with a bright future, present an influential class of electrical energy storage devices. They are promising in the widespread use of alternative renewable energy sources, electrical vehicles, and smart power grids owing to the fact that they provide clean and low-cost systems with high power density, stable cyclability, and supreme safety [1,2]. It is well understood that electrode materials constitute the soul of SCs. Therefore, it is vital to design new materials with high energy density without sacrificing power density for fabricating high-performance SCs [3,4]

Metal-organic frameworks (MOFs) are crystalline materials with open porous channels that employ coordination bonds to link inorganic ions/clusters with organic ligands to assemble three-dimensional structures [5,6]. MOFs have remarkable properties such as fascinating topologies, synthetically controllable porosity, exceptionally high accessible surface area, and facile synthesize. More interestingly, they have ability of charge storing through physicsorption on the inner surface and redox-active behavior of metal centers inside MOFs as a pseudo-capacitive material which makes them promising energy storage materials [7–10]. MOFs possessing pores, spaces, or channels that allow rapid electrolyte ion transport, and avoid steric constraints [11]. It is worth mentioning that, surface area of MOFs significantly surpasses that of activated carbons, possibly enabling them to challenge the superiority of carbon electrodes in electric double layer capacitance (EDLC) [12].

Furthermore, because of the orderly arrangement of metallic and organic components inside the MOFs crystals, they have been regarded as sacrificial templates for the production of extremely porous carbon, metal oxide, and composite materials [13]. However, low electrical conductivity and the lousy electrolyte flexibility of MOFs have been considered as their major limitations in supercapacitors fabrication [14]. MOF-derived capacitive materials have arisen as a new kind of porous structure with a well-defined shape, qualified pores and large surface area making them appropriate choices for energy storage demands [15,16].

Great interest has been assigned to the development of multicomponent nanostructures as super-capacitive materials via composing redox active materials with conductive sp2 carbon allotropes due to their appealing aspects, such as high surface area, high electrical conductivity, presence of electrochemically active surface functionalities and high wettability towards the electrolyte [17,18].

On the other hand, by developing mixed or intercalated MOFs with highly conductive materials, improved redox activity, better electrical conductivity, and improved cycle performance can be achieved against pristine MOFs or pristine MOF-derived materials [19]. In this approach using synergistic effect, two interlaced materials employed to reinforce the benefits of individual materials or effectively prevail their limitations [20,21] Carbon nanotubes (CNTs) are desirable materials in energy storage devices because of their great mechanical strength, chemical stability, high length to diameter ratio, and high conductivity [22].

Interestingly, it has been experienced that, line contact is more efficient than point contact in enhancing ion's and electron's transportation systems. Carbon nanotubes, therefore, can enhance CNTs-MOF composites' conductivity [23].

It has been approved that trivalent metals such as Al3+, Cr3+, or In3+, can improve the chemical stability towards hydrolysis of the resulting coordination frameworks [24]. Because of the low toxicity and excellent water stability of indium (III), it is a promising option for MOF construction.

MIL 68 (*M*= eg. In3+, Al3+, Cr3+) constructed with the chains of MO4(OH)2 octahedral units linked via the terephthalate organic ligands. MIL-68(M) has two types of channels with large diameter pores of 6.0 and 16 A. As described in [25], MIL-68(M) renders completely high BET surface area and high thermal stability.

In this study, we successfully synthesized the new MIL68 (In)-CNTs hierarchical nanostructure and for the first time we have investigated its ability as a promising active material for construction of a supercapacitor. In addition, by simple annealing treatment of MIL 68 (In)-CNTs, we have achieved a fine three-dimensional In2O3 porous hexagonal prisms-CNTs (In2O3PHP-CNTs) nanocomposite. There are several studies of In2O3 as a super-capacitive material with various synthesize methodologies and divers morphologies. However, to the best of the authors' knowledge, there are no reports of In2O3PHP-CNTs templated from MOF and its application towards supercapacitors. As such, we prepared MIL 68 (In) and In2O3 PHP materials without CNTs. The asprepared MIL68 (In)-CNTs, MIL68 (In), In2O3PHP-CNTs and In2O3 PHP electrodes exhibits remarkable electrochemical performances including high specific capacitances of 601, 485, 329, and 214 Fg- 1 at the scan rate of 5 mVs- 1, and cycling stability of 95.2, 92.9, 97.1, and 91 percent after 4000 charge-discharge cycles at the current density of 8 Ag- 1, respectively. MIL 68 (In)-CNTs nanocomposite in comparison with other as-synthesized electrodes presents higher specific capacitance with lower charge transfer resistance arisen from well-ordered hierarchical porous nanocomposite which provide ample active positions and short ion and electron channels. Hence, to assess the capacitive behavior of the MIL 68 (In)-CNT-based SC, we assembled a symmetric supercapacitor (SSC) device. During charge-discharge cycles, the asfabricated SSC device demonstrated remarkable gravimetric capacity of 314 Fg- 1 at the scan rate of 2 mVs- 1 and sufficient energy density of 15.3 W h kg- 1 at power density of 300 W kg- 1, as well as excellent cycling life 95% after 4000 cycles. In accordance with the results, the superb electrochemical performance of MIL 68 (In), affirmed that our attempt to use MIL 68 (In) for construction a high-performance supercapacitor has been successful. According to our study, the interweaved MIL 68 (In) with CNTs nanoplatform can be used as a promising choice for fabrication of applicable, lightweight, low cost and environmentally friendly SC.

1.1. Chemicals

1,4-benzenedicarboxylic acid, N, N-dimethylformamide (DMF(, polyvinylpyrrolidone (PVP(, multi wall carbon nanotubes (MWCNTs) (110–170 nm × 5–9 um), methanol, ethanol, sulfuric acid (H2SO4), nitric acid (HNO3), potassium hydroxide (KOH), carbon black, graphite powder (cat #332,461), and polytetrafluoroethylene (PTFE) are purchased from Sigma Aldrich. In addition, indium (III) nitrate pentahydrate **(**In (NO3)3·5H2O) is purchased from Alfa Aaser.

1.2. Synthesize procedures

1.2.1. Synthesize of hexagonal MIL 68 (In) prisms and In2O3 porous hexagonal prisms

MIL 68 (In) prism (MIL68 (In)) is prepared through a simple solvothermal method presented by Wang et al. [26]. Briefly, 100 mg of In (NO3)3·5H2O, and 100 mg of 1,4-benzenedicarboxylic acid are dissolved in 60 mL of DMF, and stirred until solids are dissolved. Next, the as-prepared solution is placed in a heating mantel regulated at 120 ◦C for 30 min. When the reaction time is passed, the flask is cooled down to the room temperature. Finally, the white precipitates are separated from the supernatant by centrifugation and washed three times with methanol and located into the vacuum oven at 80 ◦C for 8 h. Synthesize of In2O3 porous hexagonal prisms (In2O3 PHP) is performed by annealing of hexagonal MIL 68 (In) prisms in Ar flow at 500 ◦C for 2 h with a heating rate of 5̊C/min.

1.2.2. Synthesize of interweaved hexagonal MIL68 (In) prisms with CNTs, and In2O3 porous hexagonal prism-CNT hybrids

Fabrication of hexagonal MIL 68 (In)-CNTs is started by pretreatment of CNTs with a mixture of sulfuric acid and nitric acid (with ratio of 1:3) at 80 ◦C for 3 h under stirring. Modification of CNTs surface by carboxyl groups ensured the homogeneous interweaving of CNTs within and on the MOFs. The resultant activated CNTs are collected by centrifugation, and washed repeatedly with DI water. The product is then vacuum dried at 80 ◦C for 8 h. Next, 5 mg of acid-treated CNTs and 5 mg of PVP are added into 30 mL of DMF, and the mixture is ultrasonicated for 30 min to achieve to a homogeneous suspension (solution1). Thereafter, 100 mg of In (NO3)3.5 H2O is dissolved in 30 mL of DMF and added to the solution1 drop-wise. Afterward, 100 mg of the 1,4-benzene dicarboxylic acid is added to the abovementioned solution. After 2 min of stirring, the reaction flask is placed in a heating mantel which is set to 120 ◦C for 30 min. The black precipitates are centrifuged and washed with methanol three times. In2O3 porous Hexagonal prism-CNTs nanocomposite is simply prepared by annealing the MIL 68 (In)-CNTs heated at 500 ◦C for 2 h under Ar flow at a heating rate of 5 ◦C/min. The strategy for synthesizing of active materials schematically is presented in scheme 1a.

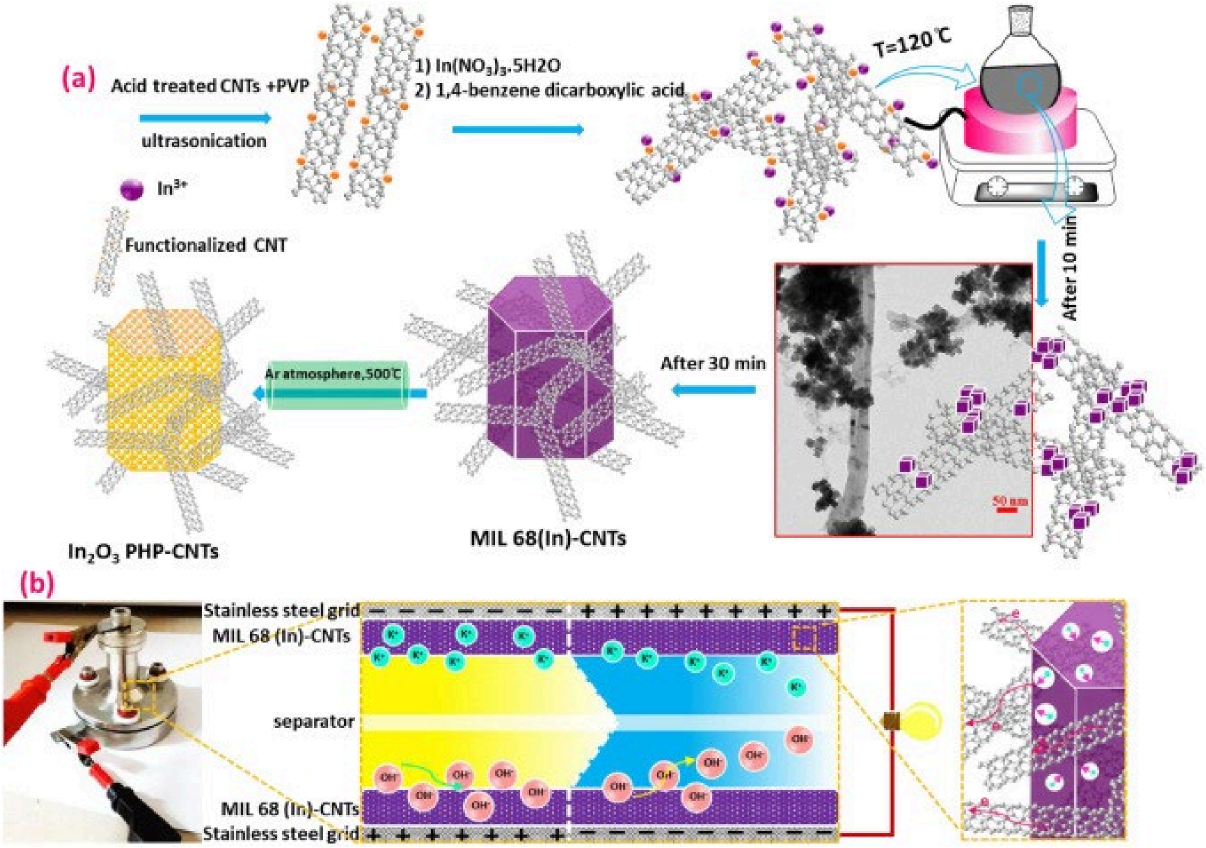

Scheme 1. (a) Synthesize route of MIL 68 (In)-CNTs and In_2O_3 PHP-CNTs; (b) illustration of integrating MIL 68 (In)-CNTs hybrid nanostructure into symmetric supercapacitor device.

3. Materials characterization

The characterization techniques that performed for achieving a wellcharacterization of as-prepared samples are as followed. Field emission scanning electron microscope (FESEM) and transmission electron microscope (TEM) are employed to examine the morphology of samples. The crystalline phase of the materials is investigated using X-ray diffraction (XRD) technique. Additionally, samples are studied via ultraviolet-visible (UV–Vis) absorption spectroscopy. Fourier transform infrared spectroscopy (FTIR) is employed to confirm the formation of MIL 68 (In). Energy-dispersive X-ray spectroscopy (EDS) is employed to illustrate the elemental distribution of the MIL 68 (In)-CNTs sample.

1.4. Electrochemical characterization

Electrochemical techniques are directed by Auto lab (PGSTAT-302 N, Eco Chemie, Netherlands) work station. NOVA 2.1.2 software is used to analyze electrochemical data. The super-capacitive performance of active materials in three electrode cells are investigated using cyclic voltammetry (CV), galvanostatic charge-discharge (GCD), and electrochemical impedance spectroscopy (EIS). The employed set up for three electrode cell contains stainless steel grid coated by the active material as a working electrode, graphite rod as a counter electrode, and Ag/AgCl electrode as a reference electrode in 3 M KOH electrolyte solution at the temperature of 25± 2̊C. Two electrode cell device of MIL68 (In)-CNTs is assembled using a Split Test Cell (MTI, 20 mm). A 25 mm thin micro porous monolayer membrane (Celgard 3501) is used as the separator. It is worth noting that in the process of fabricating the working electrode, a 75:10:10:5 wt ratio of active material, carbon black, graphite powder and polytetrafluoroethylene (PTFE), respectively, mixed using a small amount of ethanol. The resultant uniform mixture is pressed on the current collector substrate at 10 MPa. The formulas used for calculations are given in the supporting document.

Scheme 1b illustrates our method for integrating MIL 68 (In)-CNTs hybrid nanostructure into the symmetric supercapacitor device. It is based on a split cell device made up of electrodes constructed of stainless steel current collector coated by MIL 68 (In)-CNTs. The positive and negative electrodes are placed on both sides of a separator and wetted by the electrolyte solution. The positive and negative ions of the electrolyte are anticipated to flow in opposing directions across the separator and within the active material pores when the device is charged. The ions immigrate out of the pores and the electrons goes out of the device during discharge. MOFs would be suitable for this application because of their open porous framework, which provide high capacity for ion storage and strong ion cycling inside the cell [27]. Besides, introduction of hierarchy to the pores by preparation of MOFs in the presence of CNTs dispersion, upgrade the merits of the final device [28].

2. Results and discussion

2.1. Morphology and Composition characterization

SEM images of MIL 68 (In), MIL 68 (In)-CNTs, In2O3 PHP and In2O3 PHP-CNTs have been presented in Fig. 1. As it is obvious in Fig. 1a-c, the MIL 68 (In) particles have satisfactory hexagonal prism-shaped morphology. MIL 68 (In)-CNTs SEM images are presented in Fig. 1d-f. As it is shown, the CNTs encompassed the MOFs. In the cases of In2O3 PHP (Fig. 1g-i) and In2O3PHP-CNTs (Fig. 1j-l) FESEM images reveal porous hexagonal prisms that are composed of tiny nanoparticle segments interlinked tightly together in a stable framework. These images demonstrate that even after a high-temperature calcination procedure, the annealed products retain size uniformity and hexagonal prismshaped structure. The release of CO2 and H2O during heat treatment is responsible for the enhanced surface roughness and small holes on the surface of these compounds [29].

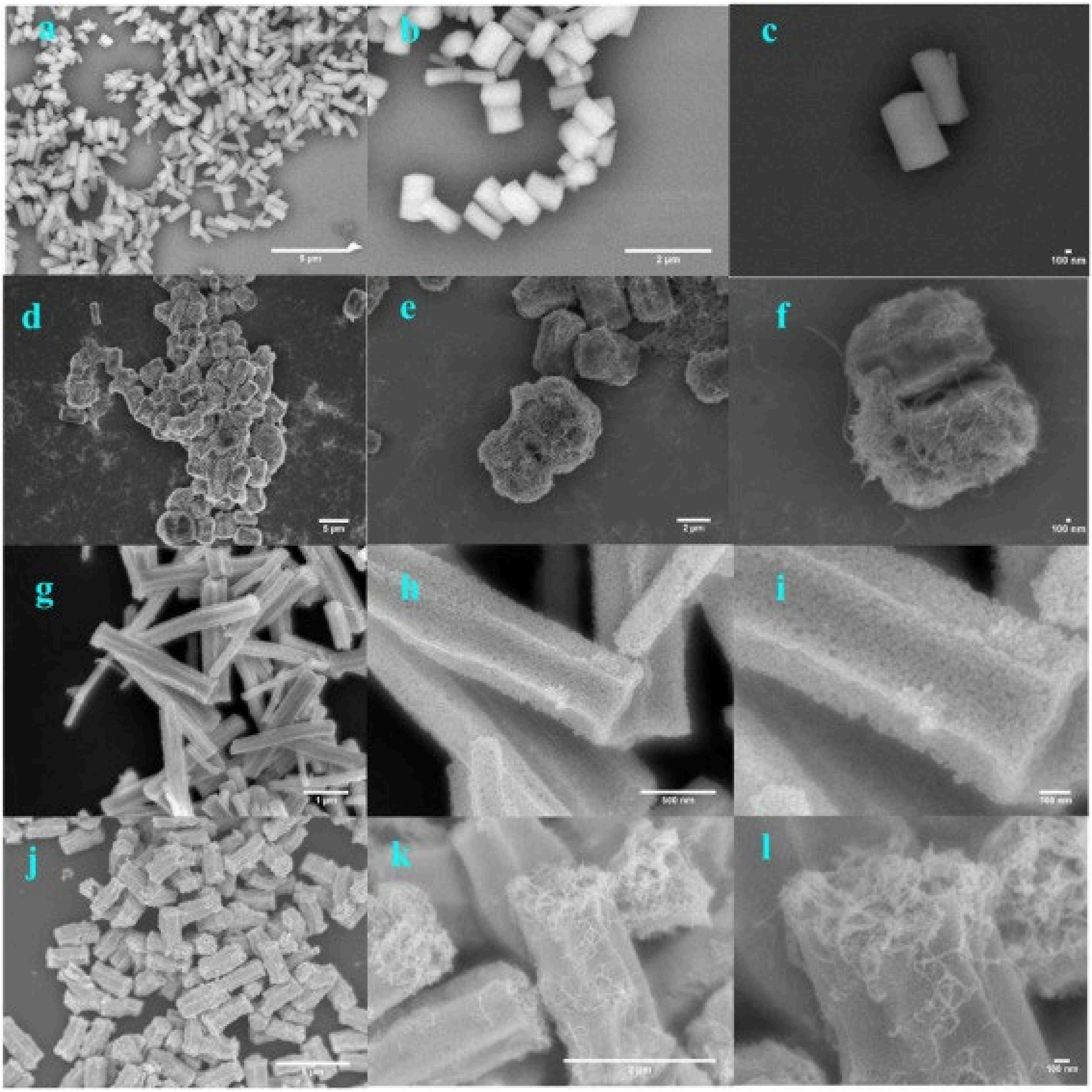

Fig. 1. FESEM images of (a-c) MIL 68 (In), (d-f) MIL 68 (In)-CNTs, (g-i) In_2O_3 PHP, (j-l) In_2O_3 PHP-CNTs at various magnifications.

The TEM images of MIL 68 (In) and In2O3 porous hexagonal prisms prepared by annealing treatment of MIL 68 (In) is presented in Fig. 2a
and b, respectively. TEM image of MIL 68 (In)-CNTs at 10 min of reaction time is captured and showed in Fig. 1S. This image demonstrates
that the –COOH functionalized CNTs provided nucleation positions for precipitation of MOFs constructing interwoven MOFs by CNTs. The TEM
image of the final product of MIL 68 (In)-CNTs at 30 min of process is presented in Fig. 2c Fig. 2.d displays a picturesque view of well-defined hexagon face of open ends of the In2O3 PHP-CNTs. Based on the TEM analyze, the porous hierarchical framework of In2O3 PHP-CNTs is evident.

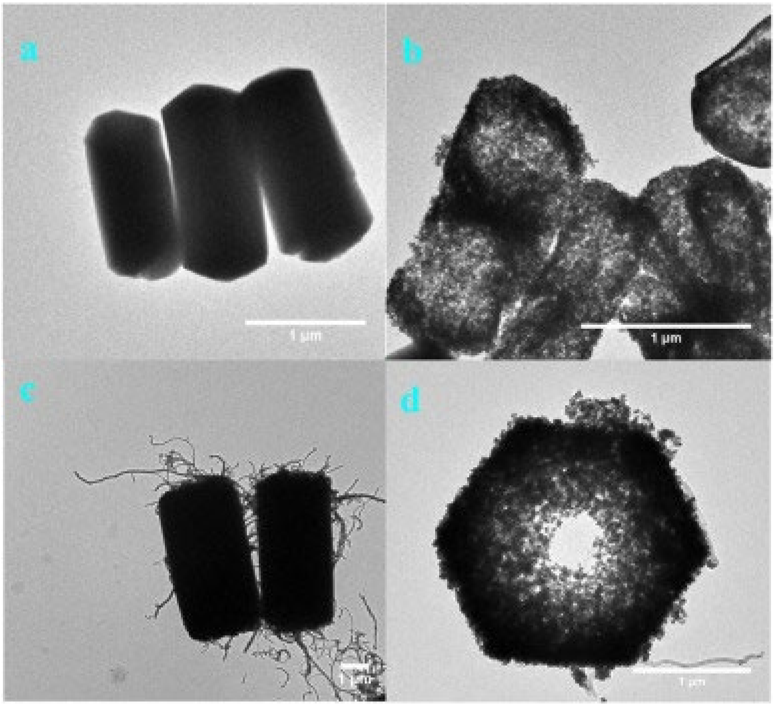

Fig. 2. TEM images of (a) MIL 68 (In), (b) In_2O_3 PHP, (c) MIL 68 (In)-CNTs, (d) In_2O_3 PHP-CNTs.

The phase purity and crystal structure of the as-synthesized samples are identified using X-ray diffraction patterns Fig. 3.a shows the XRD patterns of In2O3 PHP, In2O3 PHP-CNTs, MIL 68 (In), MIL 68 (In)-CNTs and CNTs. The patterns in Fig. 3a i, ii are indexed as cubic crystalline structure of In2O3 PHP (01–089–4595) [30]. In Fig. 3a iii, iv which demonstrates the patterns of MIL 68 (In) and MIL 68 (In)-CNTs, all the diffraction peaks are consistent with previously reported XRD diffractogram of MIL 68 (In) (96–430–6786) [25]. This confirms that the incorporation of CNTs-COOH does not disturb the crystal texture of MIL 68 (In) frameworks. In Fig. 3a v, the wide peak at around 26.5° belongs to the CNTs' characteristic (002) facet. All diffraction peaks are correlated well with the reference XRD pattern, proposing the presence of pure phase and high crystallinity of the specimens. These data revealed the simple conversion of MIL 68 (In) to In2O3 during annealing process.

The non-appeared CNTs peak within the nanocomposites patterns can be pertained to the low intensity peak of CNTs relative to high crystalline In2O3 and MIL 68 (In) platforms. To further verify the chemical structure and molecular interactions between different composites in the mixtures, MIL 68 (In), MIL 68 (In)-CNTs, In2O3 PHP and In2O3 PHP-CNTs were analyzed by Raman technique, as shown in Fig. 3b. In the same figure, the spectrum of CNTs is reported for comparison, together with the spectrum of the activated CNTs. It can be seen that the spectrum of MIL 68 (In) reveals the typical bands of MIL68 organic framework structure [31]. Two additional peaks at 1350 and 1550 cm- 1 were observed in the spectrum of MIL 68 (In)-CNTs, corresponding to the D and G bands in CNTs, respectively [32]. Further, the combination of CNTs with MIL 68 (In) might influence the surficial chemical structure by producing a compressive stress on the surficial layer of MIL 68 (In) and making the surface atoms pack closely, resulting a slight blue shift of wavenumbers of MIL 68 (In). The Raman spectrum of In2O3 PHP in the range of 600–2300 cm- 1 barely showed characteristic peaks, while the spectrum of In_2O_3 PHP-CNTs was dominated by modes associated with CNTs, indicating the existence of CNTs in this compound. Finally, a comparison between the spectra of CNTs and activated CNTs revealed that the ratio ID/IG was higher in the activated CNTs, indicating the presence of more defects in these compounds.

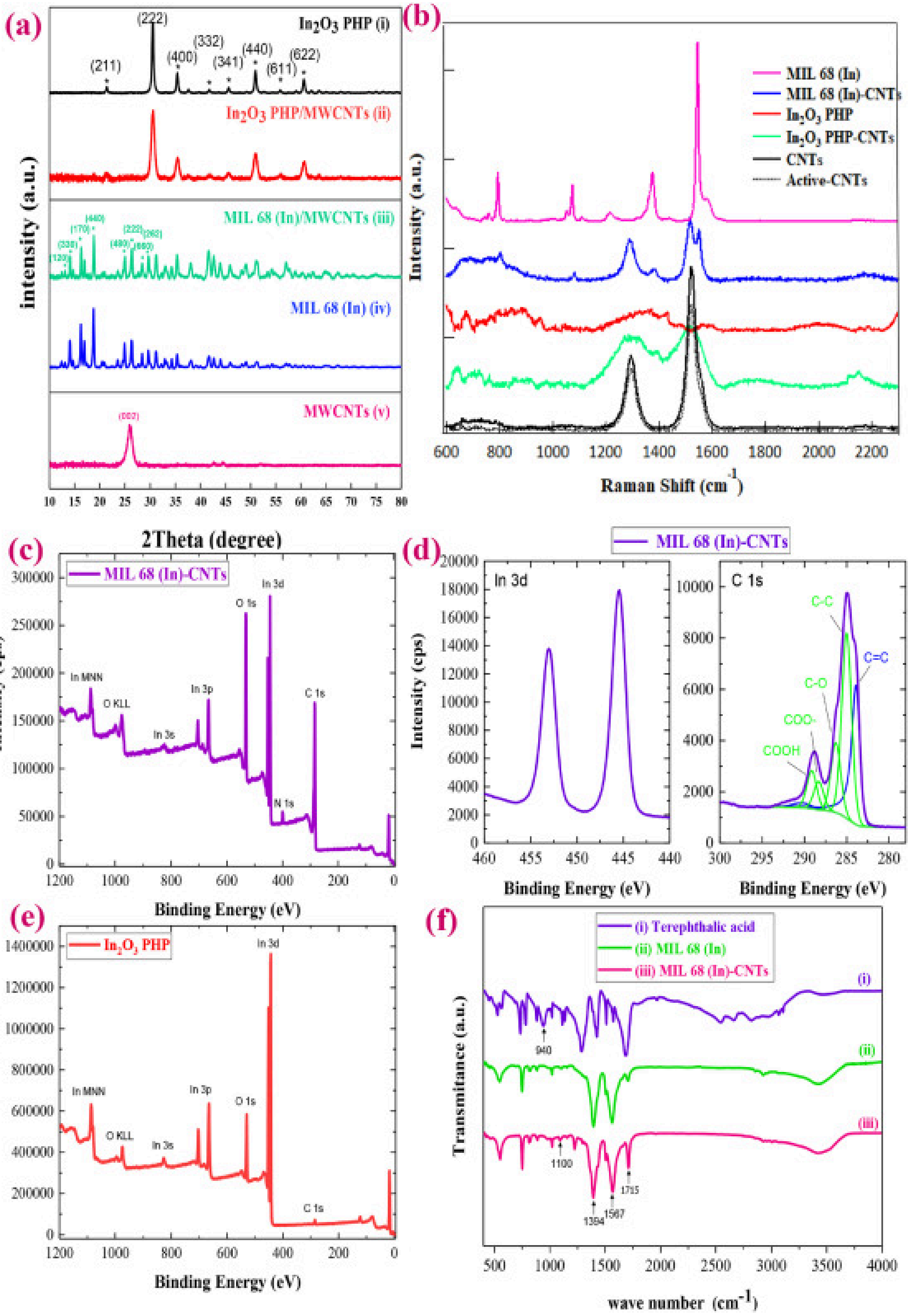

Fig. 3. XRD patterns of (a) In_2O_3 PHP, In_2O_3 PHP-CNT, MIL 68 (In), MIL 68 (In)-CNTs, and CNTs; (b) Raman spectra of the samples; (c)Wide scan on sample MIL 68 (In)-CNTs; (d) High resolution XPS on In 3d and C 1 s region; (e) Wide scan on In_2O_3 PHP; (f) FTIR spectra of MIL 68 (In), MIL 68 (In)-CNTs, and terephthalic acid.

Fig. 3c is representing the wide scan collected on MIL 68 (In)-CNTs; this spectrum reveals all the peaks that can be attributed to the MIL 68 (In)-CNTs. Besides, high resolution spectra are acquired on the In 3d and C 1 s regions which is depicted in Fig. 3d. This high resolution data show the In 3d peaks, with the main component located at ~ 445.5 eV, in line with reports of In (III) compounds [33]. Moreover, the C 1 s spectrum in Fig. 3d clearly shows the presence of CNTs, via the asymmetric *C* = *Cpeak* at ~284 eV. In this figure, the COOH groups of acid treated CNTs are also clearly detectable. Furthermore, Fig. 3e shows the wide scan which is collected on the In2O3 PHP sample. According to this figure, the data demonstrate the high purity of the sample, as the only contamination is carbon, coming from the atmosphere (so called, adventitious carbon). The O/In ratio measured by XPS is 1.6, very close to the expected value of 1.5 in stoichiometric In2O3. Indeed, the slight oxygen excess can come from the atmospheric contamination [34]. FTIR spectra of terephthalic acid, MIL 68 (In) and MIL 68 (In)-CNTs are drawn in Fig. 3f. All of the samples exhibited broad peak at around 3400 cm- 1 which is ascribed to the stretching vibration of -OH bond. The broad peak at 940 cm- 1 relates to the O–H bending vibrations of the carboxyl group in the ligand. Disappearance of O–H bend bond for MIL 68 (In) and MIL 68 (In)-CNTs has proved the absence of free ligand in the as-synthesized materials. The bands at 1394 and 1567 cm- 1 are assigned to the C–C stretching vibration from the aromatic structure [35]. The stretching vibration of the C = O groups in the carboxyl units correlates to the absorption peak at 1715 cm- 1 and the peak intensity was increased in MIL 68 (In)-CNTs which confirms the hybridization of MIL 68 (In) with MWCNTs [36]. Besides, appearance of a peak at 1100 cm- 1 attributed to the C–O stretching mode of the carboxylic acid group of MWCNTs [37,38]. The light absorption properties of the as-prepared MIL 68 (In), MIL 68 (In)-CNTs, In2O3 PHP, In2O3 PHP-CNTs, and CNTs are shown in Fig. 2S.

TGA is used to characterize MIL 68 (In) and MIL 68 (In)–CNTs samples, and determine the percent of MIL 68 (In) in the nanocomposite. It is worth noting that the thermal gravimetric analysis (TGA) is performed under Ar flow with a heating rate of 10 ◦C/min from 40 ◦C temperature to 800 ◦C as is depicted in Fig. 3S a. MIL 68 (In) partially decomposes at temperatures of 400- 500 ◦C, and CNTs do not decompose before 700 ◦C in Ar flow. From the TGA profiles (Fig. 3S a) the weight loss of 57 wt% and 49 wt% obtained for pure MIL 68 (In) and MIL 68 (In)-CNTs, respectively. Due to the presence of CNTs in MIL 68 (In)-CNTs, the weight loss is decreased compared with the MIL 68 (In). According to these results, the weight percent of MIL 68 (In) is calculated by (49 wt%/57 wt%) × 100, which is 86 wt%. Brunauer-Emmett- -Teller (BET) analysis (Fig. 3S b,c) is carried out to evaluate the specific surface area and the pore size distribution of the active materials. The specific surface area of 976 m2g- 1 and 548 m2g- 1 for MIL 68 (In)-CNTs and MIL 68 (In), respectively, verify the significant increment of surface area by hybridization of MIL 68 (In) with CNTs. Furthermore, EDX mapping analyze of MIL 68 (In)-CNTs is shown in Fig. 4S that confirms the homogeneous elemental distribution of the sample.

3. Electrochemical investigations

3.1. Three electrode set up

Here, we outlined the electrochemical charge-storage characteristics of the all synthesized platforms as working electrodes in a threeelectrode cell system to assess precisely the electrochemical performance of active materials [39].

3.1.1. CV measurements

The cyclic voltammograms of all of the as-synthesized compounds are individually recorded at varied sweep speeds to evaluate the samples' behavior as super-capacitive electrodes Fig. 4.a-d depicts the CV profiles of MIL 68 (In), MIL 68 (In)-CNTs, In2O3 PHP and In2O3 PHPCNTs in the suitable potential window of - 0.6 to 0.4, - 0.7 to 0.5, - 0.6 to 0.2, and - 0.7 to 0.3 Vs, respectively. Moreover, The CV plots at a same scan rate of 50 mVs- 1 are overlaid in Fig. 4e for observing a clear comparison. As it is depicted in Fig. 4a-d, all of the samples present the CV curves with typical pseudo-capacitive characteristics verifying platforms with rich redox active sites [40]. These findings support the presence of redox reactions of metal centers in MIL68 (In) and In2O3 PHP compounds at or near the surface of electrode. Furthermore, the CV scans produce approximately rectangular shapes and reversible mirror images. Other words, the modified electrodes have a considerable EDLC property [41].

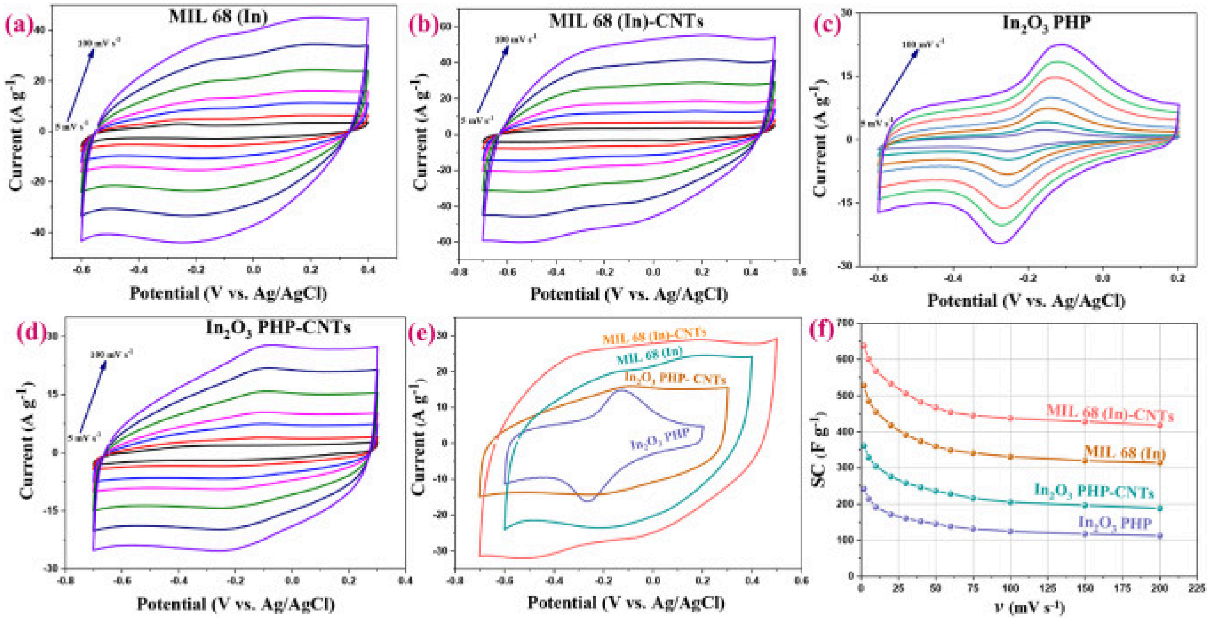

Fig. 4. CV profiles of (a) MIL 68 (In); (b) MIL 68 (In)-CNTs; (c) In_2O_3 PHP; and (d) In_2O_3 PHP-CNTs at various scan rates; (e) overlay of CV profiles of all electrodes at scan rate of 50 mVs^{-1}; (f) variation of specific capacitance as a function of scan rate.

Noticeably, even at a higher scan rate of 100 mVs- 1, the CV curves of modified electrodes indicate a nearly symmetrical rectangular form and rapid response upon voltage reversal. It is known that CV patterns with a well-defined rectangular form result in lower charge transfer resistance, and consequently, higher ion diffusion rates [42]. Besides, this imply the good reversibility of active materials which is crucial for energy-storage devices [43,44]. MIL 68 (In)-CNTs, MIL 68 (In), In_2O_3 PHP-CNTs and In_2O_3 PHP electrodes exhibits remarkable specific capacitances of 601, 485, 329, and 214 Fg^{-1} based on CV plots at the scan rate of 5 mVs^{-1}.

According to these results, the remarkable specific capacitance is achieved from direct use of MIL 68 (In) as an electrode material manifested the incorporation of large amount of pseudo-capacitive centers within the large ordered MOFs skeleton [45,46]. The findings also revealed that hexagonal In-based MOF prisms can serve as phenomenal templates to generate highly porous hollow prisms of fine In_2O_3 nanoparticles with large surface area and high active sites which can be employed as a high performance In_2O_3-based super-capacitive material [47].

A distinct difference in CV areas and optimum operating potential window is observed for hybrid materials with CNTs electrodes in comparison with pristine MIL 68 (In) and In_2O_3 PHP. This, indeed, demonstrates the key role of CNTs in the formation of excellent electric conductive and robust hybridized active networks, which can reduce ionic diffusion resistance and shortening the path length of electron gathering and transportation [14]. The percent of CNTs in the MIL 68 (In)-CNTs is 14 wt% which is calculated using the TGA analysis. Indeed, hybridization approach causes ~19% increment in the specific capacitance when compared with the pure MOF at the scan rate of 5 mVs^{-1}.

The calculated specific capacitance values as a function of scan rate of CV profiles are presented in Fig. 4f. By increasing the sweep rates, the calculated specific capacitance of all under-investigating samples will decline. This phenomena could be explained by the fact that at lower scan rates, the ions have easy access to the paths through porous materials, with abundant opportunity and time to diffuse into the electrode structure’s pores, providing lots of surfaces for faradic reactions.

Increasing the scan rates, in fact, limits the time window; therefore, the ions may only contact the electrodes’ exterior surfaces, lowering the obtained specific capacitance [48]. For the MIL 68 (In)-CNTs platform, the decrease in specific capacitance is just 34.5%, between 2 and 200 mVs^{-1} sweep rates indicating highest power characteristic among all the samples. According to the CV results, between the four examined samples, MIL 68 (In)-CNTs offered higher synergistic surface and electrochemical capacitive quality for generating larger capacitance and greater current. First reason could be related to the highest pseudo-capacitance behavior which is basically driven by the faradic reaction of indium-based MOF electroactive sites in KOH electrolyte.

Moreover, synergistic effect between two interlinked components of MIL 68 (In)-CNTs can maximize benefits of individual materials, and effectively remove their limitations leading to the most desirable behavior.

3.1.2. GCD measurements

Fig. 5 represents the galvanostatic charge and discharge analyses of four prepared electrodes at current density of 1 Ag^{-1} in optimal potential zones according to the CV measurements Fig. 5.b-e exhibits the GCD profiles for all of the samples at varied current densities from 1 to 16 Ag1. These plots revealing almost symmetric, triangular, and sharp traces. From the same durations of charging and discharging, an excellent columbic efficiency outcome of samples can be accomplished [49]. Moreover, the equilateral triangle forms of specimens suggest desirable capacitive quality and good reversibility during GCD process. This might be related to the uniform distribution of numerous metallic centers inside the MOF particles in the cases of MIL 68 (In) and, MIL 68 (In)-CNTs or fine metal oxide nanoparticles within the In2O3 PHP and In2O3

PHP-CNTs porous platforms resulting in recovered active redox processes. Besides, according to these figures, MIL 68 (In)-CNTs possess widest potential window and the longest charge-discharge time implying that the electrochemical quality of MIL 68 (In)-CNTs is significantly better than that of the other investigated samples. The calculated specific capacitance as a function of current density, ranged from 1 to 16 Ag- 1, is illustrated in Fig. 5f. Normally, with increasing current density, the corresponding capacitances will decrease, referring to the decreased ion accessibility to the pores at high current densities. Under current density of 1 Ag- 1, the MIL 68 (In)-CNTs, MIL 68 (In), In2O3 PHP-CNTs, In2O3 PHP electrodes' specific capacitance reached to the values of 473, 392, 268, and 181 Fg- 1, respectively, and subsequently 320, 240, 152, and 100 Fg- 1 (32.2, 38.7, 43.2, and 44.7% capacitance loss) at 16 Ag- 1. These findings reveal that the MIL 68(In)-CNTs electrode has more efficient and suitable electroactive locations and capability rate than the other examined cases. The results obtained here can be assigned to a larger surface area of MOFs and more available metal centers/redox active site than that of In2O3 PHP which makes it appropriate for electrochemical reactions and intercalation/de-intercalation of ions during charge storage. In addition, hybridized nanocomposites treated with CNTs indicate superb functionalities than CNTs-free composites. The composing action with CNTs offers hierarchical structures with a larger surface area advantaging in higher contact area between electrode and electrolyte, and excellent conductivity of the final nanocomposites [50].

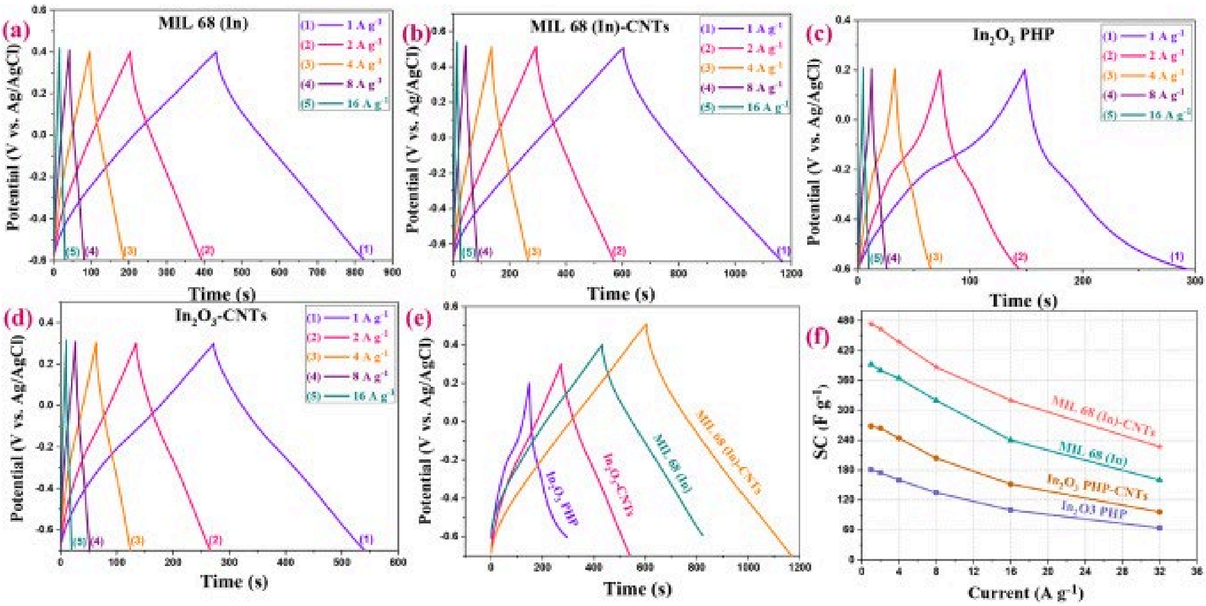

Fig. 5. GCD curves of (a) MIL 68 (In); (b) MIL 68 (In)-CNTs; (c) In_2O_3 PHP; and (d) In_2O_3 PHP-CNTs at different current densities; (e) GCD curves of all modified electrodes at 1 Ag^{-1}; (f) variation of SC as a function of current density.

Fig. 6a-d are capacitance retention versus the number of cycles conducted from the GCD evaluation of the four electrodes at 16 Ag- 1. After 4000 cycles, the measured capacitance reached to 95.2, 92.9, 97.1, and 91 percent for MIL 68 (In)-CNTs, MIL 68 (In), In2O3 PHP-CNTs, In2O3 PHP, respectively. There are two major reasons for the slightly decreased capacity after numerous charge-discharge cycles: the presence of the rapid kinetics of faradaic reactions at the electrodeelectrolyte interface [51], and frequently embedding/de-intercalate of ions at the interface of electrolyte-electrode, which leads to partially deterioration of the structures [14]. It is worth mentioning that according to the measurement results, the stability decline of electrodes is obviously restricted resulting from introduction of CNTs.

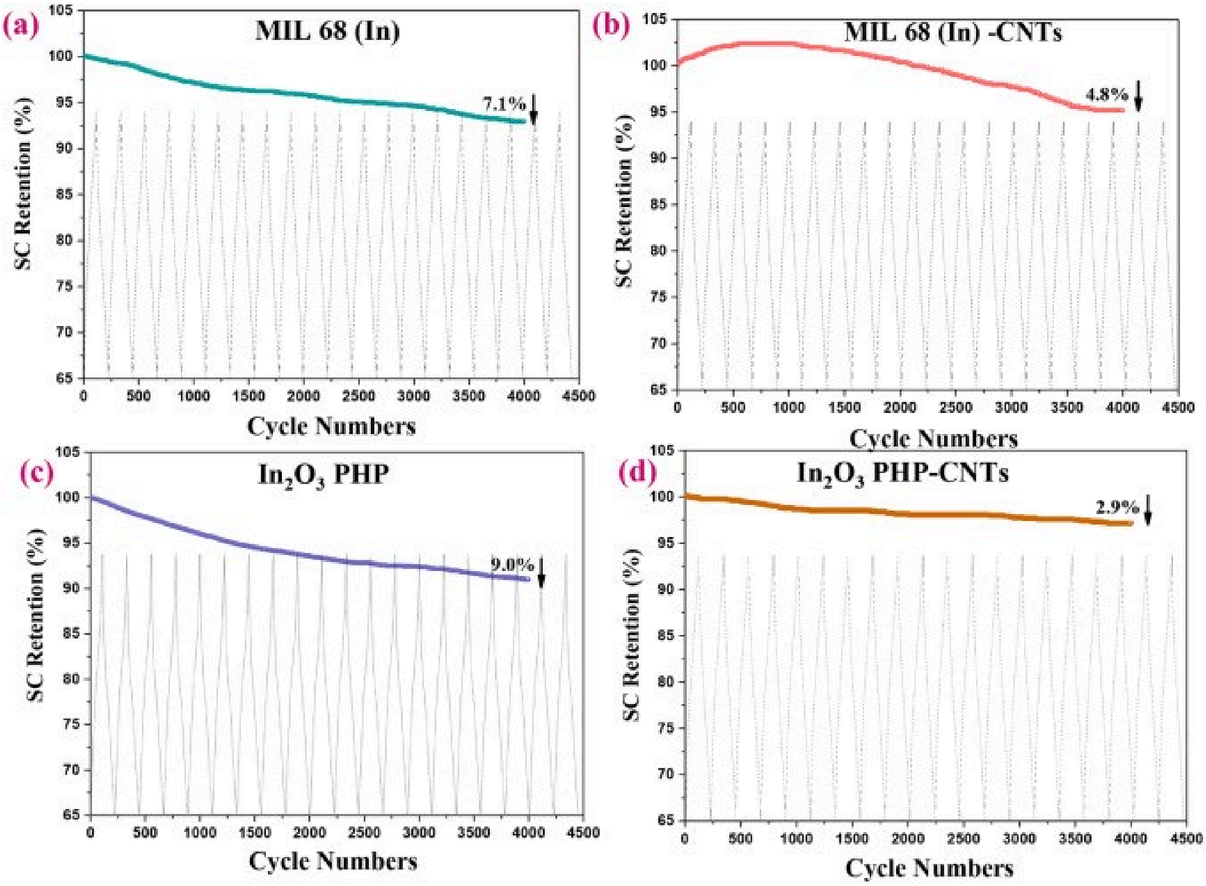

Fig. 6. Retention capacity during 4000 cycles for (a) MIL68 (In); (b) MIL68 (In)-CNTs; (c) In_2O_3 PHP; and (d) In_2O_3 PHP-CNTs at 8 Ag^{-1}.

Table 1 compares the electrochemical performance of the studied modified electrodes to that of reported In-based active materials. It can be deduced that the investigated materials demonstrate superior performance than most of the reported values in Table 1.

Table 1
Specific capacitance of indium-based capacitive materials compared to MIL 68 (In)-CNTs, MIL 68 (In), In_2O_3 PHP, and In_2O_3 PHP-CNTs.

Material	*Specific capacitance (Fg^{-1})*	*Current density/ Scan rate*	*Electrolyte*	*Cycles, Current density/ Scan rate, Retention*	*Potential range (V)*	*Ref.*
mesoporous carbon/ In_2O_3 NPs	275 (3ele)	$5 mVs^{-1}$	1 M Na_2SO_4	500, 100 mVs^{-1}, 96%	−0.6 to 0.2	[52]
In_2O_3 NPs	190 (3ele)	10 mVs^{-1}	1 M Na_2SO_3	1000, 100 mVs^{-1}, 100%	−0.6 to 0.2	[53]
In_2O_3 nanowire/CNTs	64 (2ele)	0.5 Ag^{-1}	1 M $LiClO_4$	500, 0.5 Ag^{-1}, 88%	−0.6 to 0.2	[54]
In_2O_3 nano rods	104.9 (3 ele)	8 Ag^{-1}	1 M Na_2SO_4	–	0 to −0.9	[55]
In_2O_3 nano spheres	7.6 (3ele)	8 Ag^{-1}	1 M Na_2SO_4	–	0 to −0.9	[55]
Porous In_2O_3 hollow spheres	320 (3 elec)	1 Ag^{-1}	6 M KOH	3500, @ 5 Ag^{-1}, 86%	0 to 0.45	[56]
In_2O_3 NPs/macroporous carbon	287 (3 ele)	5 mVs^{-1}	6 M KOH	5000, @ 10 mVs^{-1}, 86%	0 to 0.5	[57]
In_2O_3 /reduced graphene oxide	178.8 (3ele)	0.1 Ag^{-1}	2 M KOH	5000, @ 4 Ag^{-1}, 93.7%	−0.3 to 0.45	[58]
In_2O_3 nano discs	89.7 (2ele)	1 Ag^{-1}	1 M Na_2SO_4	10,000, @ 3 Ag^{-1}, 97%	0 to 1	[59]
In_2O_3 PHP	214 (3ele)	$5 mVs^{-1}$	3 M KOH	4000, @ 8 Ag^{-1}, 91%	−0.6 to 0.2	This work
In_2O_3 PHP-CNTs	329 (3ele)	$5 mVs^{-1}$	3 M KOH	4000, @ 8 Ag^{-1}, 97.1%	−0.7 to 0.3	This work
MIL 68 (In)	485 (3ele)	$5 mVs^{-1}$	3 M KOH	4000, @ 8 Ag^{-1}, 92.9%	−0.6 to 0.04	This work
MIL 68 (In)-CNTs	601 (3ele)	$5 mVs^{-1}$	3 M KOH	4000, @ 8 Ag^{-1}, 95.2%	−0.7 to 0.5	This work
MIL 68 (In)-CNTs	314 (2ele)	2 mVs^{-1}	3 M KOH	4000, @ 8 Ag^{-1}, 95%	0 to 1.2	This work

3.1.3. EIS measurements

To further evaluate the electrochemical behavior of the as-prepared materials, electrochemical impedance spectroscopy (EIS) analysis at frequency range of 0.01 to 100 kHz under open circuit condition is employed. Nyquist plots and the equivalent circuit of various samples are shown in Fig. 7. The obtained profiles consist of a semi-circle in the high and medium frequency region which corresponds to the chargetransfer resistance (Rct); a linear part in the middle frequency region that relates to the Warburg impedance (Zw), and a semi-vertical line at high frequency range which refers to the faradic capacitance (CF). The EIS assessments for four modified electrode are studied using the complex nonlinear least square (CNLS) fitting approach, which is applied to an equivalent circuit depicted in Fig. 7; the values of this equivalent circuit elements are provided in Table 2.

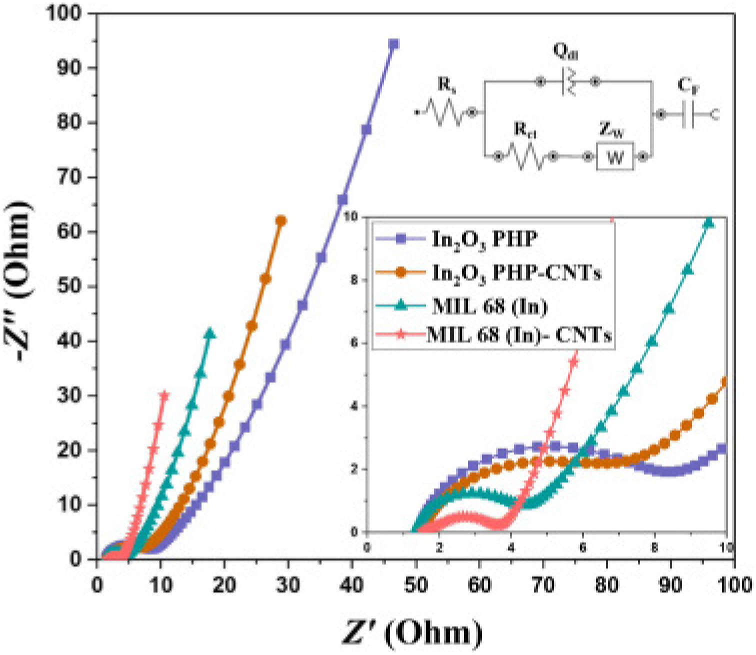

Fig. 7. The Nyquist plots of the impedance spectra of MIL 68 (In), MIL 68 (In)-CNTs, In_2O_3 PHP, and In_2O_3PHP-CNTs materials at open circuit potential.

Table 2
Data from complex nonlinear least square (CNLS) fitting approach.

	In_2O_3 *PHP*	In_2O_3 *PHP-CNTs*	*MIL 68 (In)*	*MIL 68 (In)-CNTs*
R_s	1.42	1.52	1.35	1.52
R_{ct}	6.9	5.5	3.9	2.6
Q_{dl} *(mF)*	0.59	0.77	0.53	0.44
n	0.83	0.86	0.84	0.73
W (mMho)	53	68	122	159
C_F *(mF)*	174	221	306	401

According to the data obtained from fitting, all of the modified electrodes exhibit remarkably low equivalent series and charge-transfer resistance. The diameter of the semi-circle in the profiles of hybridized with CNTs cases is notably reduced compared to that of non-hybridized cases. This confirms that the insertion of CNTs to the composites can supply an effective passageways for advantageous electron transfer, resulting in the effectively reduction of the charge-transfer resistance [60]. Additionally, MIL 68 (In)-CNTs displays the most steep slope line in the low frequency range, which is representative of highest faradic capacitance characteristic in accordance with CNLS fitting data for CF [61,62].

3.2. Two electrode set up investigations

The striking super-capacitive behavior of modified electrode with MIL 68 (In)-CNTs encouraged us to explore it in a SSC device. A view of CV measurements of MIL 68 (In)-CNTs//MIL 68 (In)-CNTs device conducted at various scan rates changing from 5 to 100 mVs- 1 with the potential window of 1.2 Vs is shown in Fig. 8a. At varying sweep speeds, the CV curves have a nearly rectangular form, indicating excellent super-capacitive behavior of SSC cell. This behavior is attributable to the electrolyte's sufficient ion concentration and the porous electrodes' exceptional electrochemical performance for rapid and effective transfer of ions. The CV plot is well retained even at the scan rates of up to 100 mVs- 1, indicating that the fabricated SSC device has a high rate capability and efficient process of charge transfer kinetics [43, 63].

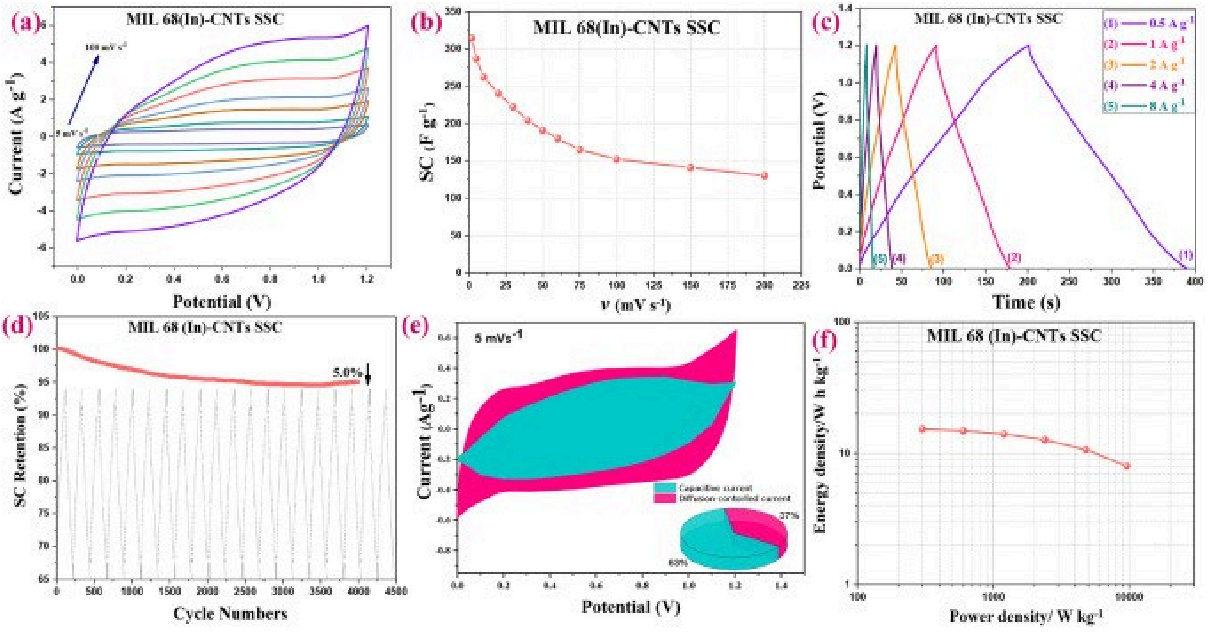

Fig. 8. (a) CV curves; (b) specific capacitance against scan rate; (c) GCD diagram; (d) Retention capacity after 4000 cycles; (e) Dunn method analysis of capacitance contribution; (f) Ragone plot, for MIL68 (In)-CNTs // MIL68 (In)-CNTs super capacitor.

Fig. 8b indicates the plots of the specific capacitance versus the scan rate. The highest specific capacitance of 314 Fg- 1 at the scan rate of 2 mVs- 1 is obtained for the SSC cell. For further assessment of the fabricated cell's performance, the galvanostatic charge-discharge profiles at different current densities are obtained and illustrated in Fig. 8c. The specific capacitance of the symmetric cell is calculated using the discharge time, which is 306 Fg- 1 at the current density of 0.5 Ag- 1. As can be seen in Fig. 8d, based on continuous charge-discharge assay, the symmetric supercapacitor device also demonstrated very good long term cycle life, with a retention capacity of about 95 percent after 4000 charge-discharge cycles (8 Ag- 1). Dunn method analysis of capacitance contribution of MIL 68 (In)-CNTs active material is exhibited in Fig. 8e. The capacitance differentiation method reveals that 63% of the total capacitance is from EDL capacitive effects. In Fig. 8e, the magenta colored region shows the pseudocapacitive and cyan colored region shows the electrical double-layer capacitive processes [64]. Fig. 8f shows the Ragone plot of the energy density versus power density of the MIL 68 (In)-CNTs SSC device calculated from Fig. 5S. The assembled SSC device can deliver a maximum energy density of 15.3 Whkg- 1 at the power density of 300 Wkg- 1, while remaining at 10.7 Whkg- 1 at the power density of 4800 Wkg- 1. The values reported for others devices are shown in Fig. 8f for comparison.

We can describe the superior achievement of the SSC device using following main reasons. First, long range order MOF with large surface area meet the qualification merits of having a high value EDLC. Second, MIL 68(In) by providing high redox active sites offers a high specific capacitive outcome. In addition, integrating a highly porous and conductive structure using hybridizing the MIL 68(In) with CNTs enhances the charge storage ability of electrodes through adsorption of a large quanta of ions and providing short ion diffusion pathway for fast ion uptake and release. All of as-mentioned merits work synergistically to guarantee the superior electrochemical performances.

4. Conclusion

In this study, we have designed the nanocomposite of interweaved MIL 68 (In) with CNTs, and In2O3 PHP-CNTs templated from this nanocomposite. We have expanded our attention to their extensive electrochemical investigation as new admirable super-capacitive electrodes.

The cell made with MIL 68 (In)-CNTs nanoplatform achieved a substantial capacitance of 314 Fg- 1, at the scan rate of 2 mVs- 1 with high energy density of 15.3 Whkg- 1 at a power density of 300 Wkg- 1, and 95% capacitance retention after 4000 charge-discharge cycles. The new-synthesized conductive hierarchical MIL68 (In)-CNTs structure has the facility of the rapid ion and electron transportation. Porous cavities in this nanocomposites serve as reservoirs for electrolyte ions during charge-discharge process. As such, fast-reversible redox behavior of indium-based electroactive sites in alkali media accelerates the charge transport kinetics, and exhibits superior electrochemical performances including a higher specific capacitance. It can be concluded that the new-designed active electrode materials meet the key requirements of high performance, low cost and light weight supercapacitors.

Author statement

F. Farbod: Idea, experiment, calculation and writing - original draft. Hamid Reza Naderi, Ali Mirvakili, Mengjiao Wang, Dipak V. Shinde, Silvia Dante, Pejman Salimi, Simone Lauciello, Mirko Prato: Experiment and calculation.

M. Mazloum-Ardakani: Idea and writing-reviewing and editing.

Declaration of Competing Interest

The authors declare that they have no known competing financial interests or personal relationships that could have appeared to influence the work reported in this paper.

Acknowledgements

The authors would like to thank Yazd University Research Council, for financial support of this research.

Supplementary materials

Supplementary material associated with this article can be found, in the online version, at doi:10.1016/j.est.2022.104238.

References

[1] V. Yang, R.A. Senthil, J. Pan, A. Khan, S. Osman, L. Wang, W. Jiang, Y. Sun, Highly ordered hierarchical porous carbon derived from biomass waste mangosteen peel as superior cathode material for high performance supercapacitor, J. Electroanal. Chem. 855 (2019), 113616, https://doi.org/10.1016/j.jelechem.2019.113616.

[2] B.E. Conway, Electrochemical Supercapacitors: Scientific Fundamentals and Technological Applications, Springer Science & Business Media, 2013.

[3] P.-C. Chen, G. Shen, S. Sukcharoenchoke, C. Zhou, Flexible and transparent supercapacitor based on In 2 O 3 nanowire/carbon nanotube heterogeneous films, Appl. Phys. Lett. 94 (2009) 43113, https://doi.org/10.1063/1.3069277.

[4] A. Khan, R. Arumugam Senthil, J. Pan, Y. Sun, X. Liu, Hierarchically porous biomass carbon derived from natural withered rose flowers as high-performance material for advanced supercapacitors, Batter. Supercaps. 3 (2020) 731–737, https://doi.org/10.1002/batt.202000046.

[5] R.R. Salunkhe, Y.V. Kaneti, Y. Yamauchi, Metal - organic framework-derived nanoporous metal oxides toward supercapacitor applications, Progr. Prospect. 11 (2017), https://doi.org/10.1021/acsnano.7b02796.

[6] N.W. Ockwig, O. Delgado-Friedrichs, M. O'Keeffe, O.M. Yaghi, Reticular chemistry: occurrence and taxonomy of nets and grammar for the design of frameworks, Acc. Chem. Res. 38 (2005) 176–182, https://doi.org/10.1021/ar020022l.

[7] H. Furukawa, K.E. Cordova, M. O'Keeffe, O.M. Yaghi, The chemistry and applications of metal-organic frameworks, Science (2013) 341, https://doi.org/10.1126/science.1230444.

[8] S. Kitagawa, Metal–organic frameworks (MOFs), Chem. Soc. Rev. 43 (2014) 5415–5418, https://doi.org/10.1039/C4CS90059F.

[9] C. Xu, X. Kong, S. Zhou, B. Zheng, F. Huo, M. Strømme, Interweaving metal–organic framework-templated Co–Ni layered double hydroxide nanocages with nanocellulose and carbon nanotubes to make flexible and foldable electrodes for energy storage devices, J. Mater. Chem. A 6 (2018) 24050–24057, https://doi.org/10.1039/C8TA10133G.
[10] F.-S. Ke, Y.-S. Wu, H. Deng, Metal-organic frameworks for lithium ion batteries and supercapacitors, J. Solid State Chem. 223 (2015) 109–121, https://doi.org/10.1016/j.jssc.2014.07.008.
[11] D.-G. Wang, Z. Liang, S. Gao, C. Qu, R. Zou, Metal-organic framework-based materials for hybrid supercapacitor application, Coord. Chem. Rev. 404 (2020), 213093, https://doi.org/10.1016/j.ccr.2019.213093.
[12] D. Sheberla, J.C. Bachman, J.S. Elias, C.-J. Sun, Y. Shao-Horn, M. Dinc˘ a, Conductive MOF electrodes for stable supercapacitors with high areal capacitance, Nat. Mater. 16 (2017) 220–224, https://doi.org/10.1038/nmat4766.
[13] R.R. Salunkhe, Y. Kamachi, N.L. Torad, S.M. Hwang, Z. Sun, S.X. Dou, J.H. Kim, Y. Yamauchi, Fabrication of symmetric supercapacitors based on MOF-derived nanoporous carbons, J. Mater. Chem. A. 2 (2014) 19848–19854, https://doi.org/10.1039/C4TA04277H.
[14] P. Wen, P. Gong, J. Sun, J. Wang, S. Yang, Design and synthesis of Ni-MOF/CNT composites and rGO/carbon nitride composites for an asymmetric supercapacitor with high energy and power density, J. Mater. Chem. A 3 (2015) 13874–13883, https://doi.org/10.1039/C5TA02461G.
[15] X. Jiang, S. Deng, J. Liu, N. Qi, Z. Chen, Metal–organic framework derived NiO/ Ni@ C composites as electrode materials with excellent electrochemical performance for supercapacitors, J. Energy Storage. 37 (2021), 102426, https://doi.org/10.1016/j.est.2021.102426.
[16] Y. Huang, L. Quan, T. Liu, Q. Chen, D. Cai, H. Zhan, Construction of MOF-derived hollow Ni–Zn–Co–S nanosword arrays as binder-free electrodes for asymmetric supercapacitors with high energy density, Nanoscale 10 (2018) 14171–14181, https://doi.org/10.1039/C8NR03919D.
[17] A.A. Ashtiani, E. Kowsari, V. Haddadi-Asl, M. Yousefi, H.R. Naderi, A. Chinnappan, S. Ramakrishna, Pseudocapacitive efficiency of covalently Cr-complex with Lhistidine-methyl ester as a ligand graphene oxide blended with conducting polymer (POAP) as electrode material in supercapacitor, J. Mol. Liq. 315 (2020), 113697, https://doi.org/10.1016/j.molliq.2020.113697.
[18] L. Chen, X. Xu, L. Wan, G. Zhu, Y. Li, T. Lu, M.D. Albaqami, L. Pan, Y. Yamauchi, Carbon-incorporated Fe3O4 nanoflakes: high-performance faradaic materials for hybrid capacitive deionization and supercapacitors, Mater. Chem. Front. 5 (2021) 3480–3488, https://doi.org/10.1039/D0QM00946F.
[19] S. Sundriyal, H. Kaur, S.K. Bhardwaj, S. Mishra, K.-H. Kim, A. Deep, Metal-organic frameworks and their composites as efficient electrodes for supercapacitor applications, Coord. Chem. Rev 369 (2018) 15–38, https://doi.org/10.1016/j.ccr.2018.04.018.

[20] R. Ranjithkumar, S.E. Arasi, P. Devendran, N. Nallamuthu, P. Lakshmanan, S. Sudhahar, A. Arivarasan, M.K. Kumar, Investigations and fabrication of Ni (OH) 2 encapsulated carbon nanotubes nanocomposites based asymmetrical hybrid electrochemical supercapacitor, J. Energy Storage. 32 (2020), 101934, https://doi.

org/10.1016/j.est.2020.101934.
[21] K. Wang, Y. Liu, Z. Ding, Z. Chen, G. Zhu, X. Xu, T. Lu, L. Pan, Controlled synthesis of NaTi2 (PO4) 3/Carbon composite derived from Metal-organic-frameworks as highly-efficient electrodes for hybrid capacitive deionization, Sep. Purif. Technol. 278 (2022), 119565, https://doi.org/10.1016/j.seppur.2021.119565.
[22] S.S. Rao, Synthesis of CNTs on ZnO/NiS composite as an advanced electrode material for high-performance supercapacitors, J. Energy Storage. 28 (2020), 101199, https://doi.org/10.1016/j.est.2020.101199.
[23] S.-F. Zheng, J.-S. Hu, L.-S. Zhong, W.-G. Song, L.-J. Wan, Y.-G. Guo, Introducing dual functional CNT networks into CuO nanomicrospheres toward superior electrode materials for lithium-ion batteries, Chem. Mater. 20 (2008) 3617–3622, https://doi.org/10.1021/cm7033855.
[24] N.N. Greenwood, A. Earnshaw, Chemistry of the Elements, Elsevier, 2012.
[25] C. Volkringer, M. Meddouri, T. Loiseau, N. Guillou, J. Marrot, G. Ferey, M. Haouas, F. Taulelle, N. Audebrand, M. Latroche, The Kagom´e topology of the gallium and indium metal-organic framework types with a MIL-68 structure: synthesis, XRD, solid-state NMR characterizations, and hydrogen adsorption, Inorg. Chem. 47 (2008) 11892–11901, https://doi.org/10.1021/ic801624v.
[26] S. Wang, B.Y. Guan, X.W.D. Lou, Construction of ZnIn2S4–In2O3 hierarchical tubular heterostructures for efficient CO2 photoreduction, J. Am. Chem. Soc. 140 (2018) 5037–5040, https://doi.org/10.1021/jacs.8b02200.
[27] M.D. Allendorf, A. Schwartzberg, V. Stavila, A.A. Talin, A roadmap to implementing metal–organic frameworks in electronic devices: challenges and critical directions, Chem. Eur. J. 17 (2011) 11372–11388, https://doi.org/10.1002/chem.201101595.
[28] R. Quintero, D.Y. Kim, K. Hasegawa, Y. Yamada, A. Yamada, S. Noda, Carbon nanotube 3D current collectors for lightweight, high performance and low cost supercapacitor electrodes, RSC Adv 4 (2014) 8230–8237, https://doi.org/10.1039/C3RA47517D.
[29] G. Huang, F. Zhang, X. Du, Y. Qin, D. Yin, L. Wang, Metal organic frameworks route to in situ insertion of Multiwalled Carbon Nanotubes in Co3 O4 Polyhedra as anode materials for lithium-ion batteries, 9 (2015) 1592–1599. https://doi.org/10.1021/nn506252u.
[30] N. Nadaud, N. Lequeux, M. Nanot, J. Jove, T. Roisnel, Structural studies of tindoped indium oxide (ITO) and In4Sn3O12, J. Solid State Chem. 135 (1998) 140–148, https://doi.org/10.1006/jssc.1997.7613.
[31] A. Jarrah, S. Farhadi, Dawson-type polyoxometalate incorporated into nanoporous MIL-101 (Cr): preparation, characterization and application for ultrafast removal of organic dyes, Acta Chim. Slov. 66 (2019) 85–102, https://doi.org/10.17344/acsi.2018.4517.
[32] K.N. Kudin, B. Ozbas, H.C. Schniepp, R.K. Prud'Homme, I.A. Aksay, R. Car, Raman spectra of graphite oxide and functionalized graphene sheets, Nano Lett 8 (2008) 36–41, https://doi.org/10.1021/nl071822y.
[33] C.J.P. Alexander, V. Naumkin, Anna Kraut-Vass, Stephen W. Gaarenstroom, NIST X-ray photoelectron spectroscopy database, Version 4.1, Natl. Inst. Stand. Technol. Gaithersburg (2012), https://doi.org/10.18434/T4T88K.
[34] T.L. Barr, S. Seal, Nature of the use of adventitious carbon as a binding energy standard, J. Vac. Sci. Technol. A Vacuum, Surf. Film 13 (1995) 1239–1246,

https://doi.org/10.1116/1.579868.
[35] Y. Wang, K. Kretschmer, J. Zhang, A.K. Mondal, X. Guo, G. Wang, Organic sodium terephthalate@ graphene hybrid anode materials for sodium-ion batteries, RSC Adv 6 (2016) 57098–57102, https://doi.org/10.1039/C6RA11809G.
[36] D. Park, H. Ju, T. Oh, J. Kim, A p-type multi-wall carbon nanotube/Te nanorod composite with enhanced thermoelectric performance, RSC Adv 8 (2018) 8739–8746, https://doi.org/10.1039/C7RA13572F.
[37] S. Kim, O. Dovjuu, S.-H. Choi, H. Jeong, J.-T. Park, Photovoltaic characteristics of multiwalled carbon nanotube counter-electrode materials for dye-sensitized solar cells produced by chemical treatment and addition of dispersant, Coatings 9 (2019) 250, https://doi.org/10.3390/coatings9040250.
[38] Y. Lv, R. Zhang, S. Zeng, K. Liu, S. Huang, Y. Liu, P. Xu, C. Lin, Y. Cheng, M. Liu, Removal of p-arsanilic acid by an amino-functionalized indium-based metal–organic framework: adsorption behavior and synergetic mechanism, Chem. Eng. J. 339 (2018) 359–368, https://doi.org/10.1016/j.cej.2018.01.139.
[39] A.J. Bard, L.R. Faulkner, Fundamentals and applications, Electrochem. Methods. John Wiley & Sons 2 (2001).
[40] Y. Gogotsi, R.M. Penner, Energy storage in nanomaterials–capacitive, pseudocapacitive, or battery-like? ACS Nano 12 (2018) 2081–2083, https://doi.org/10.1021/acsnano.8b01914.
[41] F. Farbod, M. Mazloum-Ardakani, H.R. Naderi, H. Mohammadian-Sarcheshmeh, Synthesis of a porous interconnected nitrogen-doped graphene aerogel matrix incorporated with ytterbium oxide nanoparticles and its application in superior symmetric supercapacitors, Electrochim. Acta. 306 (2019) 480–488, https://doi.org/10.1016/j.electacta.2019.03.131.
[42] S.A. Hashemi, S.M. Mousavi, H.R. Naderi, S. Bahrani, M. Arjmand, A. Hagfeldt, W.-H. Chiang, S. Ramakrishna, Reinforced polypyrrole with 2D graphene flakes decorated with interconnected nickel-tungsten metal oxide complex toward superiorly stable supercapacitor, Chem. Eng. J. 418 (2021), 129396, https://doi.org/10.1016/j.cej.2021.129396.
[43] W. Gao, D. Chen, H. Quan, R. Zou, W. Wang, X. Luo, L. Guo, Fabrication of hierarchical porous metal–organic framework electrode for aqueous asymmetric supercapacitor, ACS Sustain. Chem. Eng. 5 (2017) 4144–4153, https://doi.org/10.1021/acssuschemeng.7b00112.
[44] X. Xu, Y. Liu, M. Wang, C. Zhu, T. Lu, R. Zhao, L. Pan, Hierarchical hybrids with microporous carbon spheres decorated three-dimensional graphene frameworks for capacitive applications in supercapacitor and deionization, Electrochim. Acta. 193 (2016) 88–95, https://doi.org/10.1016/j.electacta.2016.02.049.
[45] A. Fateeva, P. Horcajada, T. Devic, C. Serre, J. Marrot, J. Gren`eche, M. Morcrette, J. Tarascon, G. Maurin, G. F´erey, Synthesis, structure, characterization, and redox properties of the porous MIL-68 (Fe) solid, Eur. J. Inorg. Chem. (2010) 3789–3794, https://doi.org/10.1002/ejic.201000486.
[46] H. Gholipour-Ranjbar, M. Soleimani, H.R. Naderi, Application of Ni/Co-based metal–organic frameworks (MOFs) as an advanced electrode material for supercapacitors, New J. Chem. 40 (2016) 9187–9193, https://doi.org/10.1039/C6NJ01449F.
[47] U.A. Khan, N. Iqbal, T. Noor, R. Ahmad, A. Ahmad, J. Gao, Z. Amjad, A. Wahab, Cerium based metal organic framework derived composite with reduced graphene

oxide as efficient supercapacitor electrode, J. Energy Storage. 41 (2021), 102999, https://doi.org/10.1016/j.est.2021.102999.
[48] A. Khan, R.A. Senthil, J. Pan, S. Osman, Y. Sun, X. Shu, A new biomass derived rodlike porous carbon from tea-waste as inexpensive and sustainable energy material for advanced supercapacitor application, Electrochim. Acta. 335 (2020), 135588, https://doi.org/10.1016/j.electacta.2019.135588.
[49] P. Suktha, P. Chiochan, A. Krittayavathananon, S. Sarawutanukul, S. Sethuraman, M. Sawangphruk, In situ mass change and gas analysis of 3D manganese oxide/ graphene aerogel for supercapacitors, RSC Adv 9 (2019) 28569–28575, https:// doi.org/10.1039/C9RA05444H.
[50] H.-I. Hsiang, C.-H. She, S.-H. Chung, Materials and electrode designs of highperformance NiCo2S4/Reduced graphene oxide for supercapacitors, Ceram. Int. 47 (2021) 25942–25950, https://doi.org/10.1016/j.ceramint.2021.05.325.
[51] Y. Zhao, Z. Song, X. Li, Q. Sun, N. Cheng, S. Lawes, X. Sun, Metal organic frameworks for energy storage and conversion, Energy Storage Mater 2 (2016) 35–62, https://doi.org/10.1016/j.ensm.2015.11.005.
[52] B.P. Bastakoti, H. Oveisi, C. Hu, K.C. Wu, N. Suzuki, K. Takai, Y. Kamachi, M. Imura, Y. Yamauchi, Mesoporous carbon incorporated with In2O3 nanoparticles as high-performance supercapacitors, Eur. J. Inorg. Chem. 7 (2013) 1109–1112, https://doi.org/10.1002/ejic.201201311.
[53] K.R. Prasad, K. Koga, N. Miura, Electrochemical Deposition of Nanostructured Indium Oxide : high-Performance Electrode Material for redox supercapacitors, 16 (2004) 1845–1847. https://doi.org/10.1021/cm0497576.
[54] P. Chen, G. Shen, S. Sukcharoenchoke, C. Zhou, P. Chen, G. Shen, S. Sukcharoenchoke, C. Zhou, Flexible and transparent supercapacitor based on In2O3 nanowire /carbon nanotube heterogeneous films Flexible and transparent supercapacitor based on In 2 O 3 nanowire / carbon nanotube heterogeneous films, 94 (2009) 3–6. https://doi.org/10.1063/1.3069277.
[55] J. Chang, W. Lee, R.S. Mane, B.W. Cho, S.-H. Han, Morphology-dependent electrochemical supercapacitor properties of indium oxide, Electrochem. Solid State Lett. 11 (2007), https://doi.org/10.1149/1.2805996.
[56] R. Kumar, A. Agrawal, T. Bhuvana, A. Sharma, Porous indium oxide hollow spheres (PIOHS) for asymmetric electrochemical supercapacitor with excellent cycling stability, Electrochim. Acta. 270 (2018) 87–95, https://doi.org/10.1016/j. electacta.2018.03.076.
[57] W. Zhang, Y. Tan, Y. Gao, J. Wu, J. Hu, S. He, A. Stein, B. Tang, In2O3 nanoparticles on three-dimensionally ordered macroporous (3DOM) carbon for pseudocapacitor electrodes, Electrochim. Acta. 176 (2015) 861–867, https://doi. org/10.1016/j.electacta.2015.07.081.
[58] X. Xu, T. Wu, F. Xia, Y. Li, C. Zhang, L. Zhang, M. Chen, X. Li, L. Zhang, Y. Liu, Redox reaction between graphene oxide and In powder to prepare In2O3/reduced graphene oxide hybrids for supercapacitors, J. Power Sources. 266 (2014) 282–290, https://doi.org/10.1016/j.jpowsour.2014.05.051.
[59] R.K. Mishra, J.H. Ryu, H. Kwon, S.H. Jin, Novel Two-Dimensional In 2 O 3 Nanodiscs for High-Rate Performance of Solid-State Symmetric Supercapacitors, Mater. Lett. 218 (2018), https://doi.org/10.1016/j.matlet.2018.01.173.
[60] R. Tian, Y. Zhou, H. Duan, Y. Guo, H. Li, K. Chen, D. Xue, H. Liu, MOF-derived hollow Co3S4 quasi-polyhedron/MWCNT nanocomposites as electrodes for

advanced lithium ion batteries and supercapacitors, ACS Appl. Energy Mater. 1 (2018) 402–410, https://doi.org/10.1021/acsaem.7b00072.

[61] L. Lei, X. Zhang, Y. Su, S. Wu, J. Shen, Metal–Organic Framework (MOF)-Assisted Construction of Core–Shell Nanoflower-like CuO/CF@ NiCoMn–OH for HighPerformance Supercapacitor, Energy & Fuels 35 (2021) 8387–8395, https://doi.org/10.1021/acs.energyfuels.1c00540.

[62] S.E.M. Pourhosseini, O. Norouzi, P. Salimi, H.R. Naderi, Synthesis of a novel interconnected 3D pore network algal biochar constituting iron nanoparticles derived from a harmful marine biomass as high-performance asymmetric supercapacitor electrodes, ACS Sustain. Chem. Eng. 6 (2018) 4746–4758, https://doi.org/10.1021/acssuschemeng.7b03871.

[63] M. Mazloum-Ardakani, H. Mohammadian-Sarcheshmeh, H. Naderi, F. Farbod, F. Sabaghian, Fabrication of a high-performance hybrid supercapacitor using a modified graphene aerogel/cerium oxide nanoparticle composite, J. Energy Storage. 26 (2019), 100998, https://doi.org/10.1016/j.est.2019.100998.

[64] J. Wang, J. Polleux, J. Lim, B. Dunn, Pseudocapacitive contributions to electrochemical energy storage in TiO2 (anatase) nanoparticles, J. Phys. Chem. C. 111 (2007) 14925–14931, https://doi.org/10.1021/jp074464w.